doi:10.1038/nature17668

Activation of the A_{2A} adenosine G-protein-coupled receptor by conformational selection

Libin Ye[1,2], Ned Van Eps[2], Marco Zimmer[2,3], Oliver P. Ernst[2,4] & R. Scott Prosser[1,2]

Conformational selection and induced fit are two prevailing mechanisms[1,2] to explain the molecular basis for ligand-based activation of receptors. G-protein-coupled receptors are the largest class of cell surface receptors and are important drug targets. A molecular understanding of their activation mechanism is critical for drug discovery and design. However, direct evidence that addresses how agonist binding leads to the formation of an active receptor state is scarce[3]. Here we use ^{19}F nuclear magnetic resonance to quantify the conformational landscape occupied by the adenosine A_{2A} receptor (A_{2A}R), a prototypical class A G-protein-coupled receptor. We find an ensemble of four states in equilibrium: (1) two inactive states in millisecond exchange, consistent with a formed (state S_1) and a broken (state S_2) salt bridge (known as 'ionic lock') between transmembrane helices 3 and 6; and (2) two active states, S_3 and $S_{3'}$, as identified by binding of a G-protein-derived peptide. In contrast to a recent study of the β_2-adrenergic receptor[4], the present approach allowed identification of a second active state for A_{2A}R. Addition of inverse agonist (ZM241385) increases the population of the inactive states, while full agonists (UK432097 or NECA) stabilize the active state, $S_{3'}$, in a manner consistent with conformational selection. In contrast, partial agonist (LUF5834) and an allosteric modulator (HMA) exclusively increase the population of the S_3 state. Thus, partial agonism is achieved here by conformational selection of a distinct active state which we predict will have compromised coupling to the G protein. Direct observation of the conformational equilibria of ligand-dependent G-protein-coupled receptor and deduction of the underlying mechanisms of receptor activation will have wide-reaching implications for our understanding of the function of G-protein-coupled receptor in health and disease.

A myriad of signalling processes associated with vision, sensory response, neurotransmitter- and hormone-mediated response, inflammation, and cell homeostasis are governed by G-protein-coupled receptors (GPCRs), also called seven transmembrane helix (7TM) receptors. A_{2A}R is a family A GPCR and an important drug target for treating inflammation, cancer, ischaemia reperfusion injury, sickle cell disease, diabetic nephropathy, infectious diseases, and neuronal disorders[5]. An understanding of the mechanism of GPCR activation and the representative conformational states is key to the drug design process. Our molecular perspective of activation is biased by X-ray crystallography, where the receptor is stabilized through thermostable mutants, fusion protein constructs, and appropriate ligands to obtain a single lowest-energy structure, often designated as either 'inactive' or 'active'. Using ^{19}F NMR and judiciously placed tags, we observed A_{2A}R in a dynamic equilibrium between two inactive and two active states. The activation process can thus be viewed from the perspective of populations of key functional states, and the action of ligands on this conformational landscape through conformational selection.

X-ray crystal structures of A_{2A}R, stabilized either by inverse agonist or by agonist, suggest that receptor activation involves a rearrangement of the 7TM bundle; that is, the inward shift of the intracellular part of TM7, a translation of TM3, and the formation of a bulge in TM5, in addition to an outward displacement and rotation of TM6 bringing together the intracellular ends of TM5 and TM6 (refs 6–8). Analogous observations were made for the β_2-adrenergic receptor[9] (β_2AR) and the light-activatable GPCR rhodopsin[10–12], suggesting a common activation pathway (Extended Data Fig. 1). Via activation intermediates through which these TM domains rearrange, GPCRs form an increasingly larger crevice at the cytoplasmic side[11], which is eventually large enough to harbour the key binding sites of interacting G protein and arrestin[9,13]. We used electron paramagnetic resonance (EPR) and NMR to identify labelling sites on TM5 and TM6. A ^{19}F NMR label at V229C on TM6 (Extended Data Figs 2 and 3) appeared to be ideal for monitoring activation of A_{2A}R (the version used in this study is truncated after residue 317). In assessing conformational states and studying conformational exchange of GPCRs on the microsecond to millisecond timescale, both ^{13}C and ^{19}F NMR have proved useful[4,14–18]. In particular, ^{19}F NMR provides exquisite sensitivity to solvent exposure or side-chain packing, often revealing a wealth of conformations[4,16,17].

A recent ^{19}F NMR study of β_2AR identified four distinct states associated with receptor activation[4]. The apo form of β_2AR was populated solely by two rapidly exchanging conformers corresponding to the 'ionic lock', a salt bridge between Arg131$^{3.50}$ on TM3 and Glu268$^{6.30}$ on TM6, either formed (S_1) or broken (S_2). An additional long-lived (lifetime $\tau = 660$ ms) β_2AR active state (S_3), in slow exchange with S_1 and S_2, was identified upon binding of agonist[4]. Further addition of a nanobody mimicking a G protein established another, fully active state (S_4) of β_2AR, deemed to be competent for signalling as concluded from the same maximally splayed cytoplasmic surface as in the β_2AR•Gα_s crystal structure[4,9]. Because neither of the two active states, S_3 and S_4, could be detected in the ligand-free apo form of β_2AR, it was not possible to distinguish between induced fit and conformational selection as models for β_2AR activation.

In contrast to β_2AR, the present ^{19}F NMR study revealed four states (two inactive and two active) associated with ligand-free apo A_{2A}R[6,8,19] (Fig. 1 and Extended Data Figs 4 and 5). Owing to striking parallels with the previous study of β_2AR, we have adopted a similar nomenclature for the states. The two inactive states S_1 and S_2 are in fast exchange on a millisecond timescale (Extended Data Fig. 4) and are represented by a single resonance, designated S_{1-2}, which in analogy to β_2AR flickers between an ionic lock stabilized (S_1) and broken state (S_2). Corresponding states are seen in A_{2A}R crystal structures: a thermostablized A_{2A}R mutant with inverse agonist bound reveals an intact ionic lock between Arg102$^{3.50}$ and Glu228$^{6.30}$ (ref. 19), whereas A_{2A}R structures with either antagonist[6] or agonist[8] bound show a broken ionic lock. Two upfield shifted resonances are associated with active states, S_3 and $S_{3'}$, as identified by binding of G-protein-derived peptides (see below). In stark contrast to β_2AR, the active states S_3 and $S_{3'}$ are already present in the A_{2A}R apo form and their populations are

[1]Department of Chemistry, University of Toronto, UTM, 3359 Mississauga Road North, Mississauga, Ontario L5L 1C6, Canada. [2]Department of Biochemistry, University of Toronto, 1 King's College Circle, Toronto, Ontario M5S 1A8, Canada. [3]Department of Technical Biochemistry, University of Stuttgart, 31 Allmandring, Stuttgart, Baden-Württemberg, D-70569, Germany. [4]Department of Molecular Genetics, University of Toronto, 1 King's College Circle, Toronto, Ontario M5S 1A8, Canada.

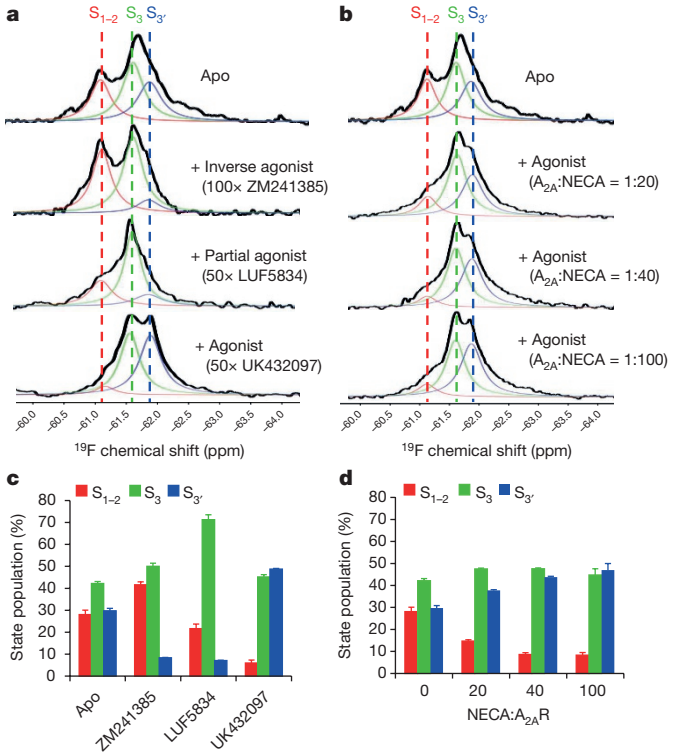

Figure 1 | Ligand-dependent $A_{2A}R$ state equilibria. Three distinct resonances of ^{19}F-labelled $A_{2A}R$-V229C are associated with inactive (S_{1-2}, shown in red) and active states (S_3, shown in green, and $S_{3'}$, shown in blue), as a function of representative ligands. **a**, ^{19}F NMR spectra of the receptor in the apo form or in the presence of inverse agonist, partial agonist, or full agonist, respectively. **b**, ^{19}F NMR spectra of the receptor in the apo form and with increasing amounts of NECA agonist. **c**, Histogram obtained from spectral deconvolutions, comparing the relative populations of S_{1-2}, S_3, and $S_{3'}$ states. **d**, Histogram comparing the relative populations of states, S_{1-2}, S_3, and $S_{3'}$, upon titration of the full agonist NECA to $A_{2A}R$. Experiments were replicated at least three times from separately expressed and reconstituted samples. Details on the chemical shift referencing, line shape fitting procedure, and error analyses are provided in the Supplementary Information and Extended Data Figs 5 and 6.

increased by the addition of partial agonist or full agonist, respectively. Addition of ligand merely alters the distribution of states in a manner consistent with conformational selection.

Figure 1 and Extended Data Fig. 6 show ^{19}F NMR spectra of 2-bromo-*N*-(4-(trifluoromethyl)phenyl) acetamide (BTFMA)-labelled $A_{2A}R$-V229C as a function of representative ligands (inverse agonist (ZM241385), partial agonist (LUF5834), and two full agonists (UK432097 and NECA)). Three resonances associated with states, S_{1-2}, S_3, and $S_{3'}$, can be identified in all of the spectra. Addition of inverse agonist shifts the equilibrium towards the S_{1-2} ensemble. Addition of the partial agonist LUF5834 stabilizes S_3. The allosteric modulator HMA has the same effect on S_3 with the caveat that the resonance associated with S_{1-2} appears to be exchange broadened (Extended Data Fig. 7). Finally, full agonists (UK432097 or NECA) shift the equilibrium towards $S_{3'}$. The chemical shifts associated with S_{1-2}, S_3, and $S_{3'}$ are observed to be increasingly upfield, consistent with a corresponding increase in solvent exposure of the probe[20] and opening of the cytoplasmic crevice via rotation and translation of TM5 and TM6. The corresponding state populations are obtained directly from signal deconvolutions (Fig. 1a, b) and are provided as histograms (Fig. 1c, d).

While inactive states S_1 and S_2 undergo exchange on a low millisecond timescale, exchange between the inactive state ensemble S_{1-2} and the active states S_3 and $S_{3'}$ is of the order of 1 or 2 s, as shown by saturation transfer experiments (Fig. 2). In this case, the inactive ensemble can be selectively saturated by application of a low power pulse applied at a frequency, ν_S, slightly downfield from the resonance associated with S_{1-2}. By recording spectra as a function of the duration of the pulse, it is possible to determine the rate of exchange between S_3 and S_{1-2}, or equivalently the lifetime of the S_3 intermediate state, τ_{S_3}. Conversely, the lifetime of the inactive ensemble, $\tau_{S_{1-2}}$, can be determined by saturating the active states (S_3 and $S_{3'}$) as described in Extended Data Fig. 8. Note that because of overlap between S_3 and $S_{3'}$, it is difficult to measure their mutual exchange. The saturation transfer experiments (Fig. 2) reveal that the S_3 state is long-lived (1–3 s) for $A_{2A}R$ in the apo form or when bound to either inverse agonist or partial agonist. The addition of agonist (UK432097) appears to shorten the lifetime of the S_3 state, which may be a consequence of lowered barriers, and, hence, exchange between S_3 and both S_{1-2} and the $S_{3'}$ states. The saturation transfer experiments are further consistent with a sequential transition $S_{3'} \rightarrow S_3 \rightarrow S_{1-2}$ (Extended Data Fig. 8b, c).

A sequence of GPCR states where the receptor becomes gradually more active has been shown for the photoreceptor and GPCR rhodopsin[3,11,12,21]. According to this sequence of reaction steps, formation of the fully active receptor state is concomitant with a proton uptake from the aqueous environment to the conserved D(E)RY motif on TM3. We therefore recorded pH-dependent ^{19}F NMR spectra of BTFMA-labelled $A_{2A}R$-V229C in the apo form and in the presence of saturating amounts of NECA agonist (Fig. 3). With decreasing pH, the population of states shifted towards the $S_{3'}$ state at the expense of S_{1-2} and S_3, as expected for a coupled equilibrium where the last transition from S_3 to $S_{3'}$ is pH-dependent. The pH-dependent population of the $S_{3'}$ state was more pronounced in the presence of NECA agonist (Fig. 3a). An analogy is seen with opsin (the apo form of rhodopsin), which is also

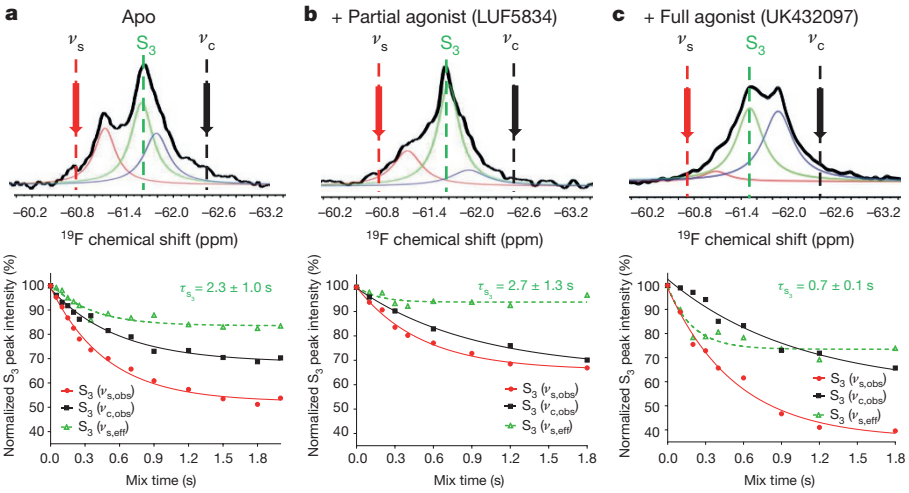

Figure 2 | Ligand-induced effects on conformational state lifetimes. ^{19}F NMR spectra of BTFMA-labelled $A_{2A}R$-V229C and corresponding decay curves associated with S_3, upon saturating S_{1-2}. **a**, $A_{2A}R$ apo form. **b**, **c**, $A_{2A}R$ in the presence of saturating amounts of partial agonist (LUF5834; **b**) or full agonist (UK432097; **c**). To account for off-resonant saturation effects due to the pulse at a frequency, ν_S, a control experiment was performed at a frequency, ν_c, equidistant to the peak of interest. The effective decay curve (green dashed line) represents the approximate response of S_3 associated with selective saturation to S_{1-2}.

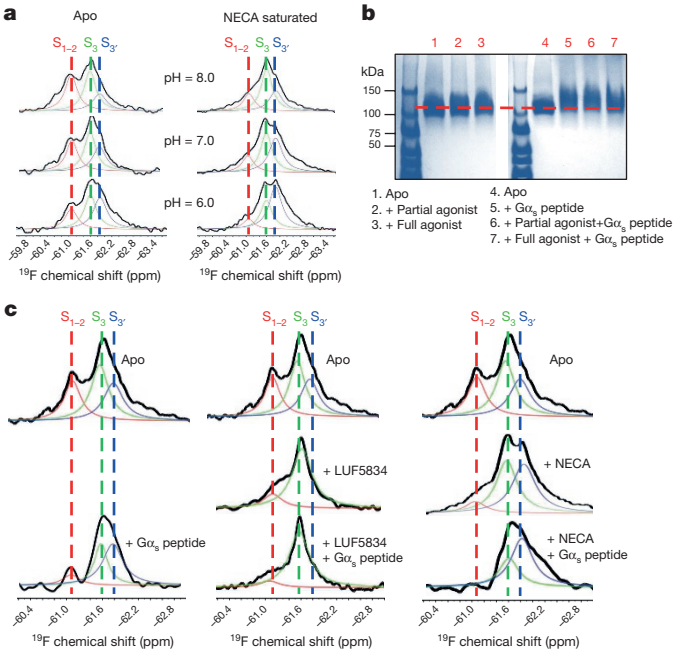

Figure 3 | Effect of pH and $G\alpha_s$-derived peptide on $A_{2A}R$ conformational states. a, ^{19}F NMR spectra of BTFMA-labelled $A_{2A}R$-V229C at various pH values for the $A_{2A}R$ apo form (left) and $A_{2A}R$ saturated with NECA agonist (right). **b**, Native gel of BTFMA-labelled $A_{2A}R$-V229C in the apo form or in the presence of saturating amounts of partial agonist (LUF5834) or full agonist (NECA), respectively (lanes 1–3). The presence of a $G\alpha_s$-derived peptide causes a mobility shift (lanes 5–7). **c**, ^{19}F NMR spectra of BTFMA-labelled $A_{2A}R$-V229C in either the apo form or in the presence of saturating amounts of partial agonist (LUF5834) or full agonist (NECA) in absence and presence of $G\alpha_s$-derived peptide. Ligand and peptide concentrations were 50 × LUF5834, 100 × NECA and 50 × $G\alpha_s$-derived peptide, respectively, relative to the receptor concentration.

in a pH-dependent equilibrium between inactive and active states[22] and where stabilization of the active state is additionally facilitated by the presence of all-*trans*-retinal agonist[12,21].

In Fig. 3b, c, we examine the effect of a peptide derived from the carboxyl (C)-terminal domain of the G-protein $G\alpha_s$ (RVF NDARDIIQRMHLRQYELL)[23] on the equilibrium of $A_{2A}R$ states. ^{19}F NMR data and mobility shifts in native gels showed that the peptide is able to interact with the apo receptor and $A_{2A}R$ saturated with partial agonist or full agonist. Addition of the peptide reduced the inactive state ensemble population and shifted the equilibrium towards the S_3 and $S_{3'}$ states, identifying both states as active as characterized by their capability to interact with the $G\alpha_s$-derived peptide. S_3 and $S_{3'}$ states have different conformations and thus may vary in their capacity to activate G protein. In the presence of saturating amounts of full agonist, addition of the $G\alpha_s$ peptide resulted in a pronounced shift towards S_3 and $S_{3'}$, whereas in the presence of partial agonist the S_3 intermediate prevailed without population of $S_{3'}$. The spectra thus demonstrate that the $G\alpha_s$ peptide is able to bind either S_3 or $S_{3'}$ states in a manner consistent with conformational selection. Moreover, a closer inspection of the apo spectrum suggests that the peptide preferentially binds to $S_{3'}$ over S_3, which is not the case in the presence of a partial agonist. Rather, the partial agonist stabilizes the S_3 state, and addition of $G\alpha_s$-derived peptide only reinforces this state. This probably directly relates to a reduced efficiency of binding and activation of the holo G protein when partial agonist stabilizes $A_{2A}R$.

The activation process associated with GPCRs is probably best understood in the case of visual rhodopsin with its covalently bound chromophore 11-*cis*-retinal[11,12,21]. Light absorption causes *cis*/*trans* isomerization and thus *in situ* conversion of an inverse agonist into an agonist. The fully active G-protein-interacting state develops sequentially through a series of metarhodopsin states which are in equilibrium and are stabilized by proton uptake. We find a remarkable similarity for $A_{2A}R$ with inactive and active states, which find their counterparts in the rhodopsin activation scheme as proposed earlier[21]. The opsin apo form exists in a pH-dependent conformational equilibrium[22] and retinal uptake is suggested to occur via conformational selection[24].

The current NMR data reaffirm the idea that key functional states simultaneously exist within a dynamic and 'loosely coupled' ensemble[25] of the unliganded receptor, as depicted in Fig. 4. Inactive and active states exchange slowly, as has been previously noted in studies of other GPCRs[4,26,27]. The corresponding high activation barriers probably

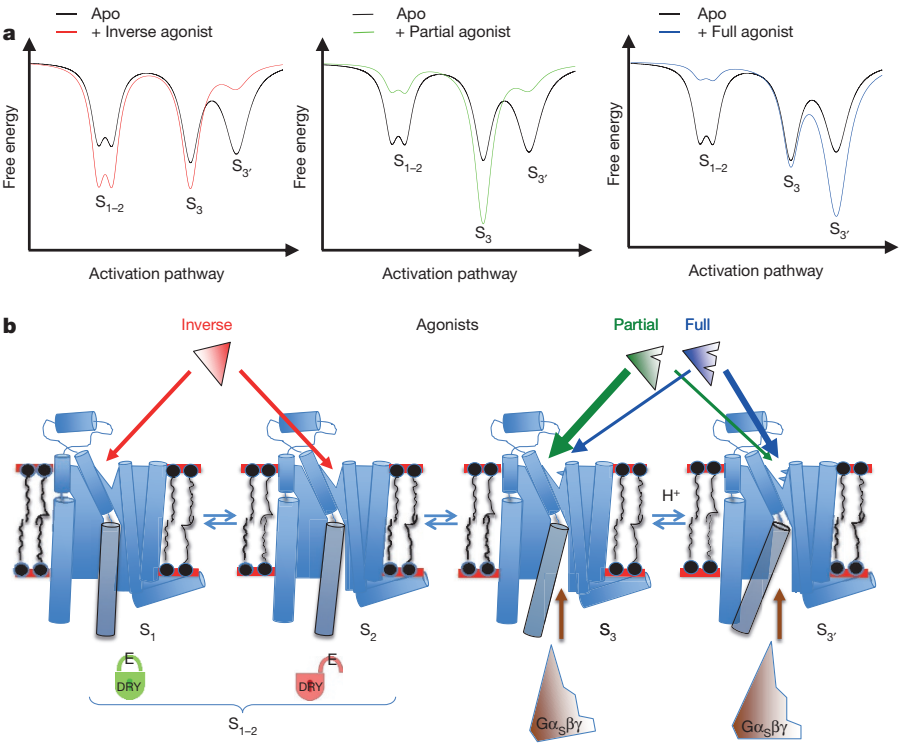

Figure 4 | Model of the free energy landscape and corresponding model of A_{2A} receptor activation. a, The effects of inverse agonist, partial agonist, and full agonist on the state equilibria are illustrated in the free energy landscapes. The functional states (S_{1-2}, S_3, and $S_{3'}$) are characterized as sitting in deep free-energy wells, while undergoing relatively slow exchange. Ligands affect this landscape in a manner consistent with conformational selection. **b**, Binding of $G\alpha_s\beta\gamma$ to apo $A_{2A}R$ is enabled through the active state ensemble. Partial agonists and full agonists either stabilize S_3 or $S_{3'}$, respectively. This gives rise to two levels of binding and activation of $G\alpha_s\beta\gamma$.

play a key role in regulation of signalling. Despite these barriers, basal activity of a receptor such as $A_{2A}R$ would be expected to occur owing to the presence of $S_{3'}$ and, presumably to a lesser extent, S_3. An inverse agonist shifts the equilibrium towards the inactive ensemble, S_{1-2}, and suppresses the basal population of active states.

The addition of partial agonist or full agonist further stabilizes the respective active states, consistent with the notion of conformational selection[28], while it is also clear that ligands influence barrier heights associated with activation, as exemplified by the observation that HMA resulted in faster exchange between S_{1-2} and S_3 (Extended Data Fig. 7). We note that 70% of the unliganded receptors adopt the active states, S_3 or $S_{3'}$, in contrast to β_2AR, where the receptor was biased towards the inactive ensemble and active states could only be detected with agonist and/or nanobody[4]. It may be that, in the absence of agonists, the active states associated with β_2AR are either very weakly populated or are short-lived and therefore exchange-broadened to the point where they cannot yet be detected. The coexistence of S_3 and $S_{3'}$ in $A_{2A}R$ also underlies the concept of partial agonism, which refers to a pharmacological phenomenon where the addition of saturating amounts of a given agonist results in sub-maximal signalling or efficacy. There are two schools of thought as to how partial agonism might originate at a molecular level. Quite simply, a partial agonist may establish an unstable (short-lived) fully active state[29]. In this case, the peak associated with a partial agonist would be represented by a weighted average between resonances associated with the fully active and other active and inactive states and might also exhibit exchange broadening. The second possibility is that a partial agonist sub-optimally engages the orthosteric binding site such that the active conformation is simply not fully established (that is, S_3 in $A_{2A}R$). The two distinct frequencies, which prevail for any ligand tested, imply the existence of two inherently stable states, whose relative populations are determined by the ligand and/or environment. The addition of partial agonist would result in a 'less open' $A_{2A}R$ conformation, leading to weaker allosteric coupling with the G protein, than that attained through the 'more open' $S_{3'}$ state. This notion that the conformation of the partial agonist stabilized state is not fully competent to engage with the G protein is reminiscent of a recent description of partial agonism in terms of the triggering of multiple switches in the receptor[30].

We note that V229C was selected as a labelling site, as discussed in the Methods, to discriminate between active and inactive states, identified by crystallography, while minimizing expression losses, misfolding, or loss of function. A survey of other domains may reveal additional nuances associated with the activation process. We have been able to demonstrate that ligand binding to $A_{2A}R$ occurs through conformational selection rather than induced fit. This has important ramifications for drug design as it implies that any therapeutic compound would ideally favour a pre-existing receptor state. Accordingly, choice of the interacting state would then dictate pharmacology.

Online Content Methods, along with any additional Extended Data display items and Source Data, are available in the online version of the paper; references unique to these sections appear only in the online paper.

Received 21 November 2015; accepted 16 March 2016.
Published online 4 May 2016.

1. Weikl, T. R. & Paul, F. Conformational selection in protein binding and function. *Protein Sci.* **23,** 1508–1518 (2014).
2. Nussinov, R., Ma, B. & Tsai, C. J. Multiple conformational selection and induced fit events take place in allosteric propagation. *Biophys. Chem.* **186,** 22–30 (2014).
3. Deupi, X. & Kobilka, B. K. Energy landscapes as a tool to integrate GPCR structure, dynamics, and function. *Physiology* **25,** 293–303 (2010).
4. Manglik, A. *et al.* Structural insights into the dynamic process of β_2-adrenergic receptor signaling. *Cell* **161,** 1101–1111 (2015).
5. Ruiz, M. L., Lim, Y. H. & Zheng, J. Adenosine A_{2A} receptor as a drug discovery target. *J. Med. Chem.* **57,** 3623–3650 (2014).
6. Jaakola, V. P. *et al.* The 2.6 angstrom crystal structure of a human A_{2A} adenosine receptor bound to an antagonist. *Science* **322,** 1211–1217 (2008).
7. Lebon, G. *et al.* Agonist-bound adenosine A_{2A} receptor structures reveal common features of GPCR activation. *Nature* **474,** 521–525 (2011).
8. Xu, F. *et al.* Structure of an agonist-bound human A_{2A} adenosine receptor. *Science* **332,** 322–327 (2011).
9. Rasmussen, S. G. *et al.* Crystal structure of the β_2 adrenergic receptor–Gs protein complex. *Nature* **477,** 549–555 (2011).
10. Choe, H. W. *et al.* Crystal structure of metarhodopsin II. *Nature* **471,** 651–655 (2011).
11. Hofmann, K. P. *et al.* A G protein-coupled receptor at work: the rhodopsin model. *Trends Biochem. Sci.* **34,** 540–552 (2009).
12. Ernst, O. P. *et al.* Microbial and animal rhodopsins: structures, functions, and molecular mechanisms. *Chem. Rev.* **114,** 126–163 (2014).
13. Kang, Y. *et al.* Crystal structure of rhodopsin bound to arrestin by femtosecond X-ray laser. *Nature* **523,** 561–567 (2015).
14. Kofuku, Y. *et al.* Efficacy of the β_2-adrenergic receptor is determined by conformational equilibrium in the transmembrane region. *Nature Commun.* **3,** 1045 (2012).
15. Nygaard, R. *et al.* The dynamic process of β_2-adrenergic receptor activation. *Cell* **152,** 532–542 (2013).
16. Liu, J. J., Horst, R., Katritch, V., Stevens, R. C. & Wüthrich, K. Biased signaling pathways in β_2-adrenergic receptor characterized by ^{19}F-NMR. *Science* **335,** 1106–1110 (2012).
17. Kim, T. H. *et al.* The role of ligands on the equilibria between functional states of a G protein-coupled receptor. *J. Am. Chem. Soc.* **135,** 9465–9474 (2013).
18. Sounier, R. *et al.* Propagation of conformational changes during μ-opioid receptor activation. *Nature* **524,** 375–378 (2015).
19. Doré, A. S. *et al.* Structure of the adenosine A_{2A} receptor in complex with ZM241385 and the xanthines XAC and caffeine. *Structure* **19,** 1283–1293 (2011).
20. Sykes, B. D., Weingarten, H. I. & Schlesinger, M. J. Fluorotyrosine alkaline phosphatase from *Escherichia coli*: preparation, properties, and fluorine-19 nuclear magnetic resonance spectrum. *Proc. Natl Acad. Sci. USA* **71,** 469–473 (1974).
21. Okada, T., Ernst, O. P., Palczewski, K. & Hofmann, K. P. Activation of rhodopsin: new insights from structural and biochemical studies. *Trends Biochem. Sci.* **26,** 318–324 (2001).
22. Vogel, R. & Siebert, F. Conformations of the active and inactive states of opsin. *J. Biol. Chem.* **276,** 38487–38493 (2001).
23. Mazzoni, M. R. *et al.* A $G\alpha_s$ carboxyl-terminal peptide prevents G_s activation by the A_{2A} adenosine receptor. *Mol. Pharmacol.* **58,** 226–236 (2000).
24. Schafer, C. T. & Farrens, D. L. Conformational selection and equilibrium governs the ability of retinals to bind opsin. *J. Biol. Chem.* **290,** 4304–4318 (2015).
25. Dror, R. O. *et al.* Pathway and mechanism of drug binding to G-protein-coupled receptors. *Proc. Natl Acad. Sci. USA* **108,** 13118–13123 (2011).
26. Bockenhauer, S., Fürstenberg, A., Yao, X. J., Kobilka, B. K. & Moerner, W. E. Conformational dynamics of single G protein-coupled receptors in solution. *J. Phys. Chem. B* **115,** 13328–13338 (2011).
27. Vafabakhsh, R., Levitz, J. & Isacoff, E. Y. Conformational dynamics of a class C G-protein-coupled receptor. *Nature* **524,** 497–501 (2015).
28. Kumar, S., Ma, B., Tsai, C. J., Sinha, N. & Nussinov, R. Folding and binding cascades: dynamic landscapes and population shifts. *Protein Sci.* **9,** 10–19 (2000).
29. Lape, R., Colquhoun, D. & Sivilotti, L. G. On the nature of partial agonism in the nicotinic receptor superfamily. *Nature* **454,** 722–727 (2008).
30. Ahuja, S. & Smith, S. O. Multiple switches in G protein-coupled receptor activation. *Trends Pharmacol. Sci.* **30,** 494–502 (2009).

Supplementary Information is available in the online version of the paper.

Acknowledgements This work was supported by the Natural Sciences and Engineering Research Council of Canada, research discovery award grant number 261980 (to R.S.P.) and the Canada Excellence Research Chair Program (to O.P.E., who is the Anne and Max Tanenbaum Chair in Neuroscience at the University of Toronto). We thank T. Kobayashi and R. Grisshammer for providing plasmids with $A_{2A}R$ sequence. We thank J. Wells, S. Larda, and F. Huang from the University of Toronto, as well as S. Furness, B. K. Kobilka, and R. Sunahara for their suggestions and comments.

Author Contributions L.Y., O.P.E., and R.S.P. designed the research. L.Y. performed the molecular biology work, generated high-yield transformants, and optimized receptor expression and purification. L.Y. also performed NMR and EPR labelling, NMR experiments, and analysed spectroscopy data. N.V.E. performed and analysed data from EPR experiments. M.Z. assisted with cell culture and receptor purification. R.S.P., L.Y., and O.P.E. prepared the manuscript. O.P.E. and R.S.P. supervised the project.

Author Information Reprints and permissions information is available at www.nature.com/reprints. The authors declare no competing financial interests. Readers are welcome to comment on the online version of the paper. Correspondence and requests for materials should be addressed to O.P.E. (oliver.ernst@utoronto.ca) or R.S.P. (scott.prosser@utoronto.ca).

METHODS

No statistical methods were used to predetermine sample size. The experiments were not randomized. The investigators were not blinded to allocation during experiments and outcome assessment.

Plasmid construction and transformation. The full-length human $A_{2A}R$ gene, originating from construct pPIC9K_ADORA2A[31], was provided by T. Kobayashi. The construct M-TEV-hA2aRTr316-H10 (with a TEV protease cleavage site insert) was engineered from the construct M-hA2aARTr316-H10, which was provided by R. Grisshammer[32]. A gene fragment, F_α–Factor–Flag–TEV-A2aARTr316-H10, with components derived either from pPIC9K_ADORA2A or from M-TEV-hA2aRTr316-H10 was amplified by fusion PCR with primers listed in Extended Data Table 1. pPIC9K_ADORA2A and F_α-Factor–Flag–TEV-A2aARTr316-H10 were digested with BamHI-HF and NotI-HF (New England Biolabs) restriction enzymes. The isolated F_α-Factor–Flag–TEV-A2aARTr316-H10 fragment was subcloned into the pPIC9K plasmid to generate the new plasmid pPIC9K_F_α-Factor–Flag–TEV-A2aARTr316-H10. The construct pPIC9K_F_α-Factor–Flag–TEV-A2aARTr316-H10_V229C containing the V229C mutation was generated using a QuikChange Lightning Site-Directed Mutagenesis Kit (Agilent Technologies) with primers listed in Extended Data Table 1. All constructs were sequenced by a local DNA sequencing facility (The Centre for Applied Genomics, Sick Kids Hospital, Toronto, Canada) with the AOX1 primer pair of PF_{AOX1} and PR_{AOX1}, listed in Extended Data Table 1. The proteins resulting from plasmids pPIC9K_F_α-Factor–Flag–TEV-A2aARTr316-H10 and pPIC9K_F_α-Factor–Flag–TEV-A2aARTr316-H10_V229C were designated as $A_{2A}R$ (Pro2 to Ala317) and $A_{2A}R$-V229C (Pro2 to Ala317 including the V229C mutation), respectively, on the basis of their correspondence to the wild-type sequence. Freshly prepared competent cells of a strain of *Pichia pastoris* SMD 1163 (*Δhis4 Δpep4 Δprb1*, Invitrogen) were electro-transformed with PmeI-HF (New England Biolabs) linearized plasmids using a Gene Pulser II (Bio-Rad). High-copy clone selection was performed as previously described[33], and a high-yield construct was then screened by an immunoblotting assay for further expression.

Receptor expression, purification and labelling. A pre-cultured single colony on YPD (1% (w/v) yeast extract, 2% (w/v) peptone and 2% (w/v) glucose) plates containing 0.1 mg ml^{-1} G418 was inoculated into 4 ml YPD medium and cultured at 30 °C for 12 h, then transferred into 200 ml BMGY medium (1% (w/v) yeast extract, 2% (w/v) peptone, 1.34% (w/v) YNB (yeast nitrogen base) without amino acids, 0.00004% (w/v) biotin, 1% (w/v) glycerol, 0.1 M PB (phosphate buffer) at pH 6.5) and cultured at 30 °C for another 24 h with an absorbance $A_{595\,nm}$ in the range 2–6. The cell pellets were spun down at 4,000*g* for 5 min and were then resuspended in 1 l of BMMY medium (1% (w/v) yeast extract, 2% (w/v) peptone, 1.34% (w/v) YNB without amino acids, 0.00004% (w/v) biotin, 0.5% (w/v) methanol, 0.1 M phosphate buffer at pH 6.5, 0.04% (w/v) histidine and 3% (v/v) DMSO, 10 mM theophylline) at 20 °C. Methanol (0.5% (v/v)) was added every 18 h. Sixty hours after induction by methanol, cells were harvested for purification.

The cell pellets were collected by centrifugation at 4,000*g* for 10 min, and washed twice with washing buffer (50 mM HEPES, 10% glycerol, pH 7.4) before addition of breaking buffer (50 mM HEPES, pH 7.4, 100 mM NaCl, 2 mM EDTA, 10% glycerol, 100 U Zymolyase, 100 μM theophylline). The sample was kept at room temperature (20 °C) for 1 h before disruption by vortexing for 2 h at 4 °C. Intact cells and cell debris were separated from the membrane suspension by low speed centrifugation (8,000*g*) for 30 min. The supernatant was collected and centrifuged at 100,000*g* for 1 h, and the precipitated cell membrane was then immediately dissolved in membrane lysis buffer (50 mM HEPES, pH 7.4, 100 mM NaCl, 1% MNG-3 (lauryl maltose neopentyl glycol) and 0.2% CHS (cholesteryl hemisuccinate), 100 μM theophylline, and 20 mM imidazole) under continuous agitation for 1–2 h at 4 °C until the membrane was dissolved. Subsequently, Talon resin (Clontech) was added to the solubilized membranes and incubated for at least 2 h or overnight under gentle agitation.

The $A_{2A}R$-bound Talon resin was washed twice with 50 mM HEPES buffer, pH 7.4, containing 100 mM NaCl, 0.1% MNG-3, and 0.02% CHS and resuspended in the same buffer, followed by addition of 100 μM TCEP reducing agent and incubation for 20 min. TCEP was washed out immediately by two rinsing steps with a buffer made of 50 mM HEPES, pH 7.4, 100 mM NaCl, 0.1% MNG-3, and 0.02% CHS. The $A_{2A}R$-bound Talon resin was then resuspended in buffer made of 50 mM HEPES, pH 7.4, 100 mM NaCl, 0.1% MNG-3, and 0.02% CHS, and combined with 10- to 20-fold excess of the NMR label (2-bromo-*N*-(4-(trifluoromethyl)phenyl)acetamide, BTFMA)[4,34] or EPR label (3-(2-iodoacetamido)-PROXYL) in the presence of nitrogen and under gentle agitation overnight at 4 °C. At the same time, 20 μl of TEV enzyme was added to remove the $A_{2A}R$ amino (N)-terminal tag. Another aliquot of NMR label was then added and incubated for an additional 6 h to ensure complete labelling. After the labelling and removal of the N-terminal tag was complete, the $A_{2A}R$-bound Talon resin was extensively washed in a disposable column with buffer containing 50 mM HEPES, pH 7.4, 100 mM NaCl, 0.1% MNG-3, and 0.02% CHS, and apo $A_{2A}R$ was then eluted from the Talon resin with 50 mM HEPES, pH 7.4, 100 mM NaCl, 0.1% MNG-3, and 0.02% CHS, 250 mM imidazole and concentrated to a volume of 5 ml. NaCl and imidazole in the sample were then removed by dialysis against 100 ml of 50 mM HEPES, pH 7.4, 0.1% MNG-3, 0.02% CHS for 3 h. The XAC-agarose gel (antagonist xanthine amine congener (XAC) conjugated to Affi-Gel 10 resin) and $A_{2A}R$ were then incubated together for 2 h under gentle agitation. Functional $A_{2A}R$ was eluted with 50 mM HEPES, pH 7.4, 0.1% MNG-3, 0.02% CHS, 100 mM NaCl, 20 mM theophylline. The eluted samples were concentrated to 20 ml by centrifugal filtration (molecular weight cut-off 3.5 kDa), and Talon resin was added and incubated under gentle agitation for another 2 h to bind functional $A_{2A}R$. Functional $A_{2A}R$ bound to the resin was washed extensively with buffer containing 50 mM HEPES, pH 7.4, 100 mM NaCl, 0.1% MNG-3, 0.02% CHS, and 20 mM imidazole, to remove all theophylline. Then, functional apo $A_{2A}R$ was eluted with elution buffer (50 mM HEPES, pH 7.4, 100 mM NaCl, 0.1% MNG-3 and 0.02% CHS, 250 mM imidazole) and the sample was dialysed to remove imidazole and concentrated for NMR or EPR.

Choosing labelling sites based on X-ray crystal structures. PROSHIFT software[35] (http://www.meilerlab.org/index.php/servers/show?s_id=9) was used to predict Cα chemical shift differences between the crystal structures of the active NECA-bound state (Protein Data Bank (PDB) accession number 2YDV) and the inactive ZM241385-bound state (PDB accession number 3EML). For the present study, we focused on differences associated with transmembrane domains TM3, TM5, and TM6, in an effort to characterize different active states.

Double electron–electron resonance and continuous wave EPR experiments. Site $V229C^{6.31}$ was spin-labelled with 3-(2-iodoacetamido)-PROXYL to generate a paramagnetic nitroxide side chain. X-band continuous wave (CW)-EPR data of the spin-labelled apo $A_{2A}R$ were acquired using a Bruker ELEXSYS E500 CW-EPR spectrometer coupled to an ER 4123D dielectric resonator. The field sweep for data collection was 100-G and modulation amplitude was 2-G. Data sets were typically averages of 30–50 scans. Double electron–electron resonance (DEER) spectroscopy was used to verify that only a single EPR active spin label was attached to $A_{2A}R$. The identical sample as in the continuous wave experiment was used to collect Q-band DEER data using a Bruker ELEXSYS E580 spectrometer. Data were analysed using the program 'LongDistances' developed by C. Altenbach, which is available for download at http://www.biochemistry.ucla.edu/biochem/Faculty/Hubbell.

NMR experiments. NMR samples typically consisted of 250 μl volumes of 50–200 μM ^{19}F-labelled $A_{2A}R$-V229C in 50 mM HEPES buffer and 100 mM NaCl, doped with 10% D_2O. The receptor was stabilized in 0.1% MNG-3 and 0.02% CHS. All ^{19}F NMR experiments were performed on a 600 MHz Varian Inova spectrometer using a cryogenic triple resonance probe, with the high-frequency channel tuneable either to ^{1}H or to ^{19}F. Typical experimental setup included a 23 μs 90° excitation pulse, an acquisition time of 200 ms, a spectral width of 15 kHz, and a repetition time of 1 s. Most spectra were acquired with 15,000 scans, which provided a signal-to-noise ratio of roughly 100. Processing typically involved zero filling, and exponential apodization equivalent to 15 Hz line broadening.

T_2 measurements. ^{19}F-labelled apo $A_{2A}R$-V229C (200 μM; comprising amino acids 2–317) in the buffer as described above was used for measurements of transverse relaxation time (T_2) by a CPMG T_2 pulse sequence, using a refocusing period of 133 μs, with a total transverse magnetization evolution time of 0.4, 0.8, 1.2, 1.6, 2.0, 2.4, 2.8, 3.2, and 3.6 ms.

^{19}F saturation transfer experiments. To investigate slow exchange between resolved states, ^{19}F chemical exchange saturation transfer NMR experiments were performed, in which a series of continuous-wave irradiation pulses were applied both at an on-resonance frequency (ν_s) and at an off-resonance frequency (ν_c), to assess chemical exchange during steady-state saturation and off-resonant saturation effects, as shown in Fig. 2. Upon saturating the resonance associated with state B, the ideal magnetization response of A may be described by the formula[36]

$$M_t^A = M_0^A\left(\frac{k_{AB}}{\rho_A + k_{AB}}\exp[-\tau(\rho_A + k_{AB})] + \frac{\rho_A}{\rho_A + k_{AB}}\right),$$

assuming off-resonant effects are accounted for. Note that both the exchange rate constants, k_{AB}, and the longitudinal relaxation rate of spin A, ρ_A, can in principle be calculated from a fit of the above equation to the experimental data. Accordingly, the lifetime τ_A can be calculated from $\tau = 1/k_{AB}$. All fits were performed using Gnuplot (http://www.gnuplot.info).

31. André, N. *et al.* Enhancing functional production of G protein-coupled receptors in *Pichia pastoris* to levels required for structural studies via a single expression screen. *Protein Sci.* **15,** 1115–1126 (2006).

32. Weiß, H. M. & Grisshammer, R. Purification and characterization of the human adenosine A_{2a} receptor functionally expressed in *Escherichia coli*. *Eur. J. Biochem.* **269,** 82–92 (2002).
33. Scorer, C. A., Clare, J. J., McCombie, W. R., Romanos, M. A. & Sreekrishna, K. Rapid selection using G418 of high copy number transformants of *Pichia pastoris* for high-level foreign gene expression. *Bio/Technology* **12,** 181–184 (1994).
34. Ye, L., Larda, S. T., Frank Li, Y. F., Manglik, A. & Prosser, R. S. A comparison of chemical shift sensitivity of trifluoromethyl tags: optimizing resolution in ^{19}F NMR studies of proteins. *J. Biomol. NMR* **62,** 97–103 (2015).
35. Meiler, J. PROSHIFT: protein chemical shift prediction using artificial neural networks. *J. Biomol. NMR* **26,** 25–37 (2003).
36. Helgstrand, M., Härd, T. & Allard, P. Simulations of NMR pulse sequences during equilibrium and non-equilibrium chemical exchange. *J. Biomol. NMR* **18,** 49–63 (2000).
37. Ballesteros, J. A. & Weinstein, H. Integrated methods for the construction of three-dimensional models and computational probing of structure-function relations in G protein-coupled receptors. *Methods Neurosci.* **25,** 366–428 (1995).

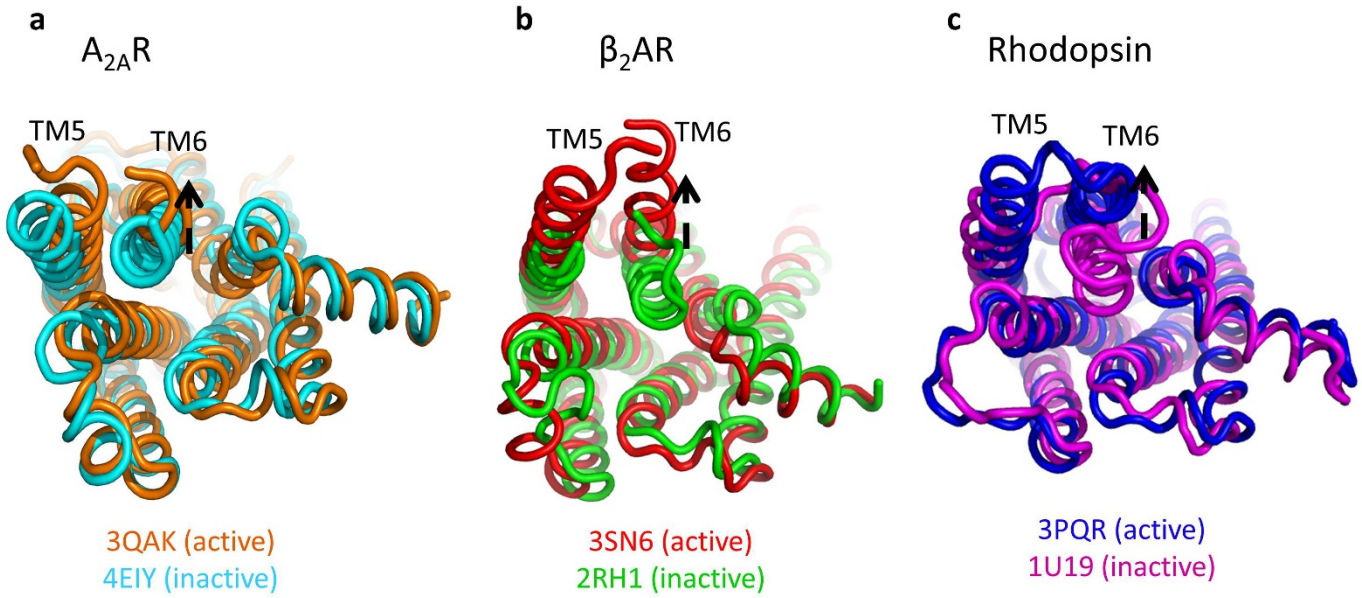

Extended Data Figure 1 | Comparison of inactive and active GPCR crystal structures. a, Inactive state $A_{2A}R$ (cyan, inverse agonist ZM241385 bound, PBD accession number 4EIY) and active state $A_{2A}R$ (brown, agonist UK432097 bound, PDB accession number 3QAK). **b**, Inactive state β_2AR (green, inverse agonist carazolol bound, PDB accession number 2RH1) and active state β_2AR (red, agonist (8-[(1R)-2-{[1,1-dimethyl-2-(2-methylphenyl)ethyl] amino}-1-hydroxyethyl]-5-hydroxy-2H-1,4-benzoxazin-3(4H)-one) bound, PDB accession number 3SN6). **c**, Inactive rhodopsin (purple, inverse agonist 11-*cis*-retinal bound, PDB accession number 1U19) and active metarhodopsin II (blue, agonist all-*trans*-retinal bound, PDB accession number 3PQR).

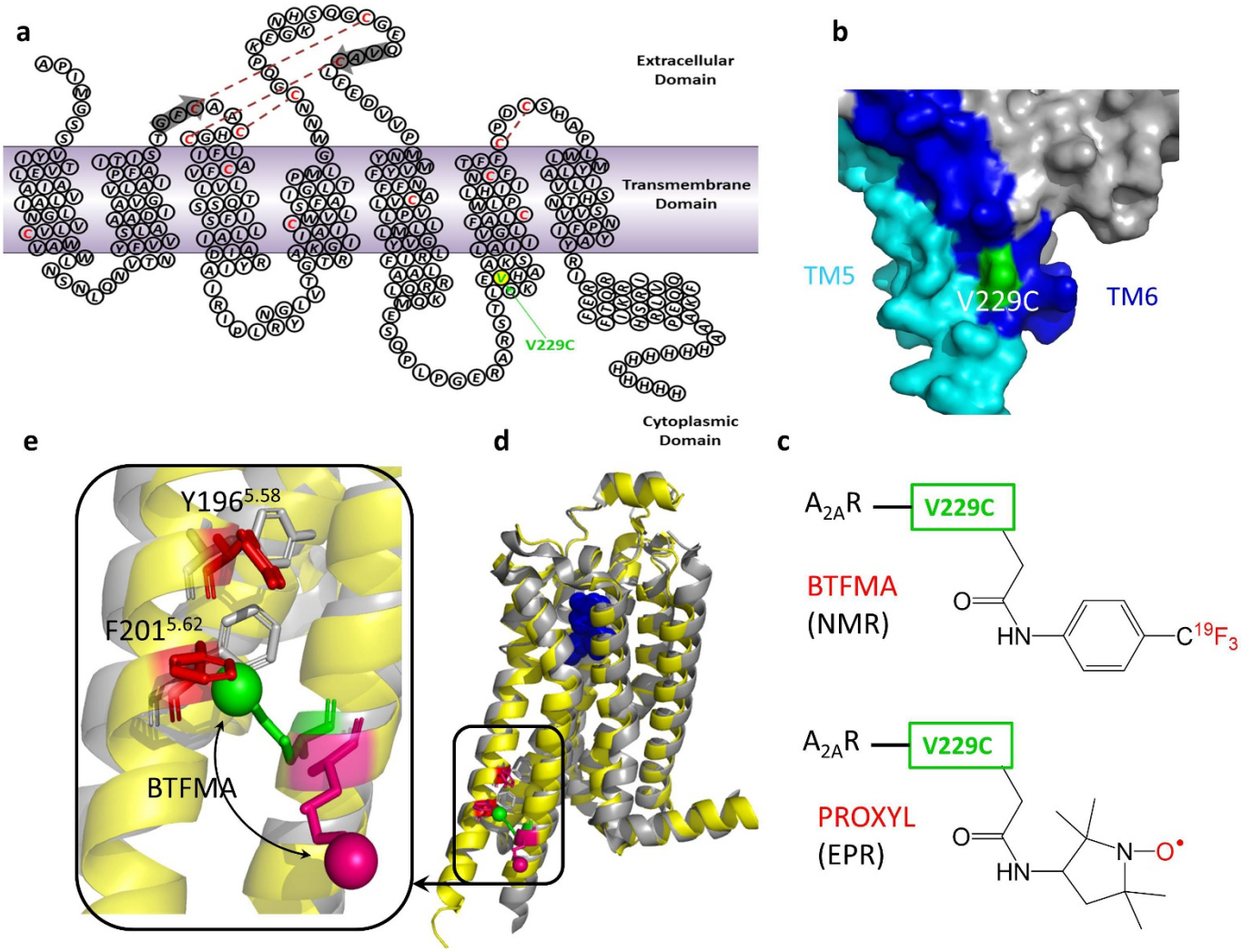

Extended Data Figure 2 | Secondary structure and topology of C-terminally truncated $A_{2A}R$-V229C. Residues 2–317 of $A_{2A}R$ are preceded by an Ala residue resulting from TEV protease cleavage, and are succeeded by an Ala–His_{10} sequence. $A_{2A}R$ was expressed in *P. pastoris* (SMD1163 strain) through genomic integration of a pPIC9K vector with a leader sequence consisting of α-Factor, Flag tag (DYKDDDDK), and a TEV protease recognition domain (SNNNNNNNNNNLGENLYFQGA). During the secretion process, the signal peptide of the α-Factor gets cleaved and the domain associated with the Flag tag and TEV recognition domain is removed by TEV protease. **a**, The truncated wild-type receptor used in this study contains all four native disulfide bonds and six buried cysteine residues (indicated in red), none of which were perturbed by the labelling process, which was specific for the introduced (solvent-exposed) cysteine residue $V229C^{6.31}$ (shown in green with yellow background; the superscript refers to the Ballesteros–Weinstein numbering[37]). **b**, A surface map suggests V229C (green, solvent exposed) should be fully labelled without perturbing the receptor. **c**, Structures of protein-attached labels for NMR (BTFMA; 2-bromo-*N*-(4-(trifluoromethyl)phenyl)acetamide) and EPR (PROXYL; 3-(2-iodoacetamido)-PROXYL) analysis. **d**, **e**, Location and topology of the labelling site associated with V229C for both the inverse agonist (inactive, grey) and agonist-bound (active, yellow) states (PDB accession numbers 4EIY and 3QAK). Two rotamers of the BTFMA label are indicated in green and purple (the phenyl moiety is shown as a sphere). Note that the size of the tags is slightly larger than that depicted in the figure. The environment around the tag is predicted to differ for inactive and active states of the receptor.

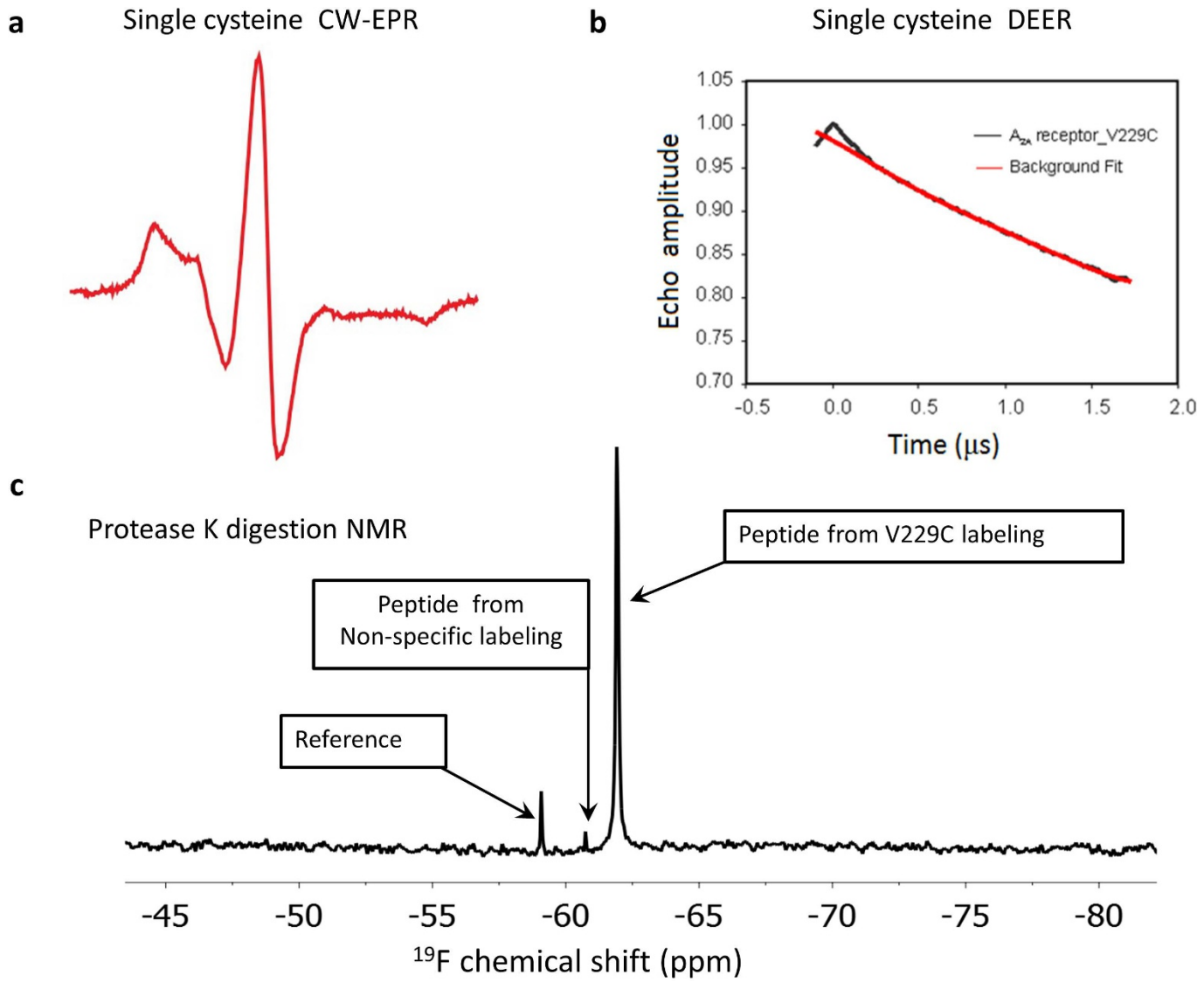

Extended Data Figure 3 | Labelling efficiency of A_{2A}R-V229C. a, Single cysteine CW-EPR spectrum of 50 μM apo A_{2A}R-V229C receptor, labelled with a PROXYL spin-label and reconstituted into MNG-3 detergent micelles. **b**, DEER measurement of 50 μM PROXYL spin-labelled apo A_{2A}R-V229C receptor. **c**, ^{19}F NMR spectra of protease-K-digested ^{19}F-labelled A_{2A}R-V229C, showing one dominant peak.

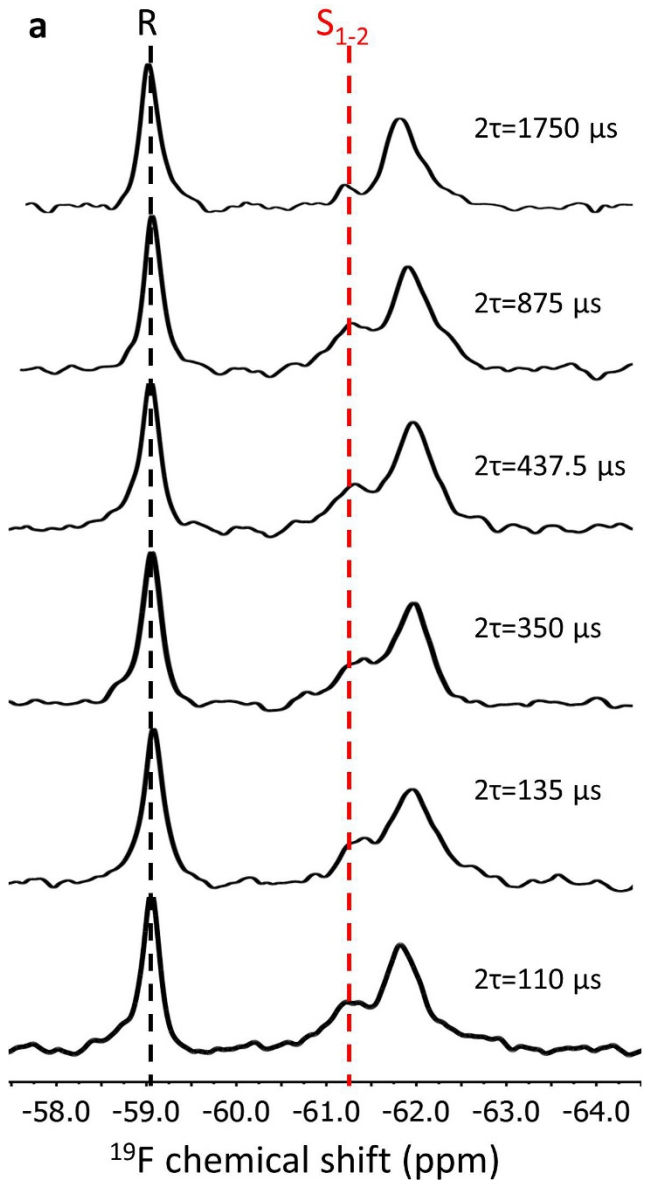

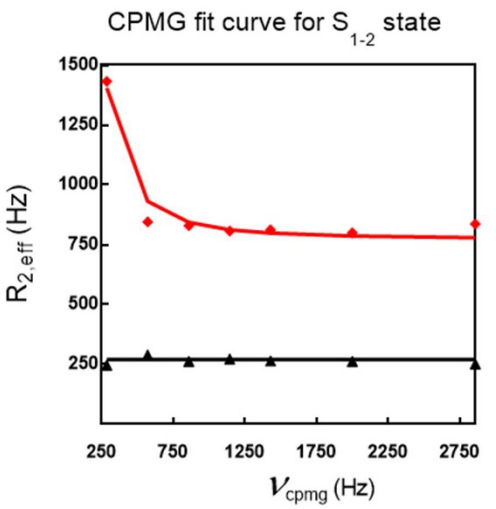

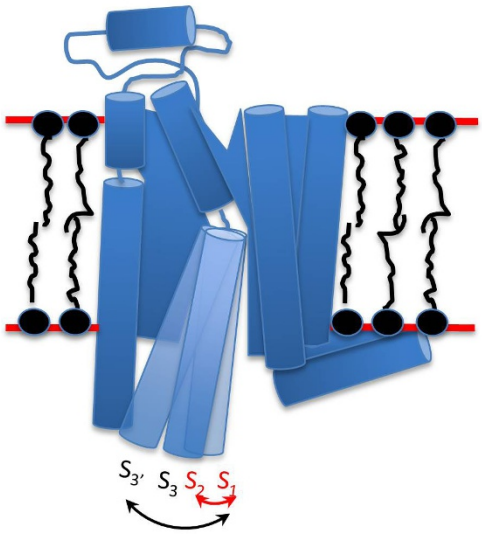

Extended Data Figure 4 | Car–Purcell–Meiboom–Gill (CPMG) relaxation dispersion experiment to evaluate dynamics of S_{1-2}. **a**, ^{19}F NMR CPMG relaxation series of ^{19}F-labelled apo A_{2A}R-V229C. Each spectrum was acquired using 10,000 scans with a constant T_2-refocusing period of 3.5 ms. The spectra in the relaxation series were recorded with different refocusing frequencies (that is, different periods between the refocusing pulses as indicated above, representative of three experiments). The sample consisted of 200 μM ^{19}F-labelled apo A_{2A}R-V229C in 50 mM HEPES buffer (pH 7.4) and 100 mM NaCl. **b**, CPMG curve for the S_{1-2} peak (red diamonds) and reference peak (black triangles). S_{1-2} undergoes millisecond timescale exchange while the reference peak exhibits no dispersion. **c**, Cartoon illustrating S_1 and S_2 exchange in addition to the activation intermediates.

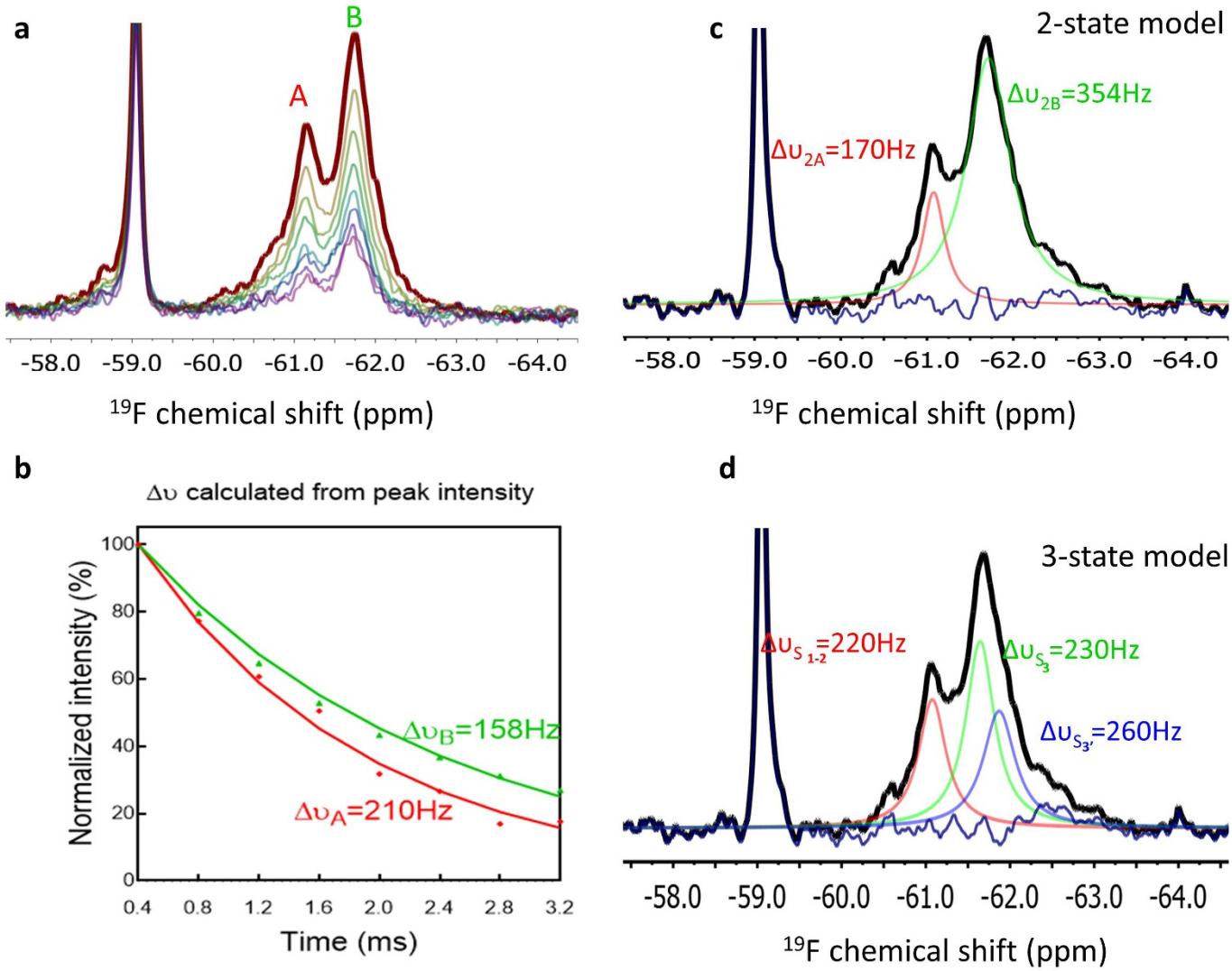

Extended Data Figure 5 | Comparison of two- and three-state models of ^{19}F-labelled A_{2A}R-V229C. a, ^{19}F NMR T_2 relaxation series of the ^{19}F-labelled apo A_{2A}R-V229C receptor. **b**, Exponential fit to T_2 for the downfield and upfield resonances, A and B in **a**. **c**, Deconvolution of the ^{19}F NMR spectrum for ^{19}F-labelled apo A_{2A}R-V229C receptor assuming a two-state model. The fitted line width of the upfield resonance is roughly twice that estimated from the T_2 measurement, suggesting the upfield resonance may be better represented as a superposition of two Lorentzian lines, associated with S_3 and $S_{3'}$, as discussed in the Supplementary Information. **d**, Spectral deconvolution of the ^{19}F NMR spectrum of the ^{19}F-labelled apo A_{2A}R-V229C receptor assuming three states. Note that the most downfield peak is ascribed to S_{1-2}, which results from the rapid flickering of the ionic lock from 'on' (S_1) to 'off' (S_2), as evidenced by the CPMG measurements in Extended Data Fig. 4. Thus, we propose a total of four states, three of which may be spectroscopically resolved. The resonance frequencies chosen in the fit for S_3 and $S_{3'}$ were based on the observed peaks seen in the presence of agonists and those identified at pH 6, where S_3 and $S_{3'}$ are better resolved. The fitted line widths are also comparable to the homogeneous line widths, estimated from the above T_2 experiment. Note that the difference spectrum (that is, the experimental spectrum minus spectral deconvolution) associated with the fit is shown in blue in **c** and **d**.

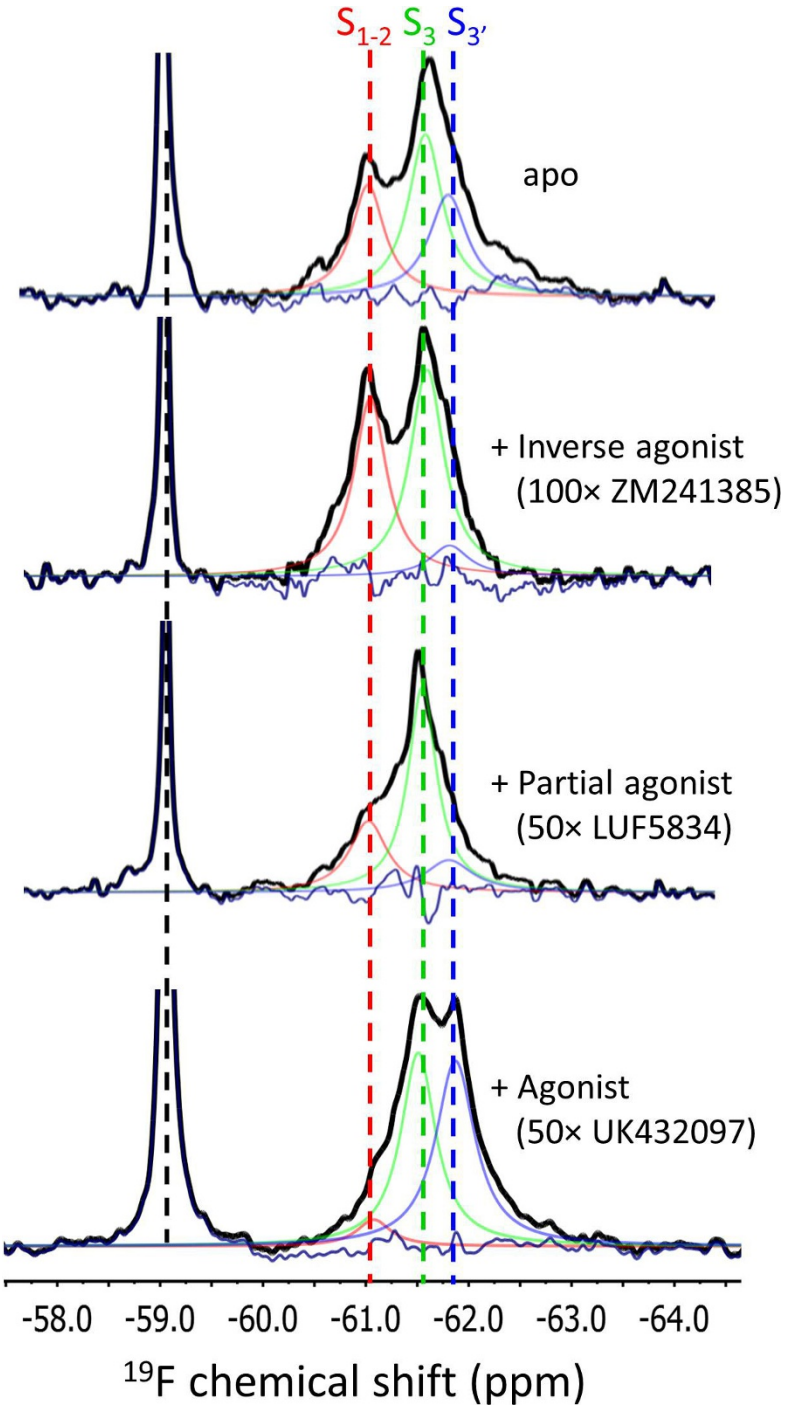

Extended Data Figure 6 | ^{19}F NMR spectra of ^{19}F-labelled A_{2A}R-V229C in the presence of 50- or 100-fold excess of different ligands. Representative ($N = 3$) ^{19}F NMR spectra as a function of ligands (inverse agonist (ZM241385), partial agonist (LUF5834), and full agonists UK432097, as shown in Fig. 1a. The downfield peak represents a reference peak resulting from the addition of 10 μM bendroflumethazide. Note that a difference spectrum (shown in dark blue), corresponding to the difference between the sum of the three deconvolved resonances and the observed spectrum, is shown in each case. Note that the chemical shifts in the deconvolutions were referenced to the standard (−59.050 ppm) and estimated to be −61.08 ppm (S_{1-2} (red)), −61.60 ppm (S_3 (green)), and −61.85 ppm ($S_{3'}$ (blue)), respectively. Corresponding line widths were estimated to be 220 Hz, 230 Hz, and 260 Hz, respectively.

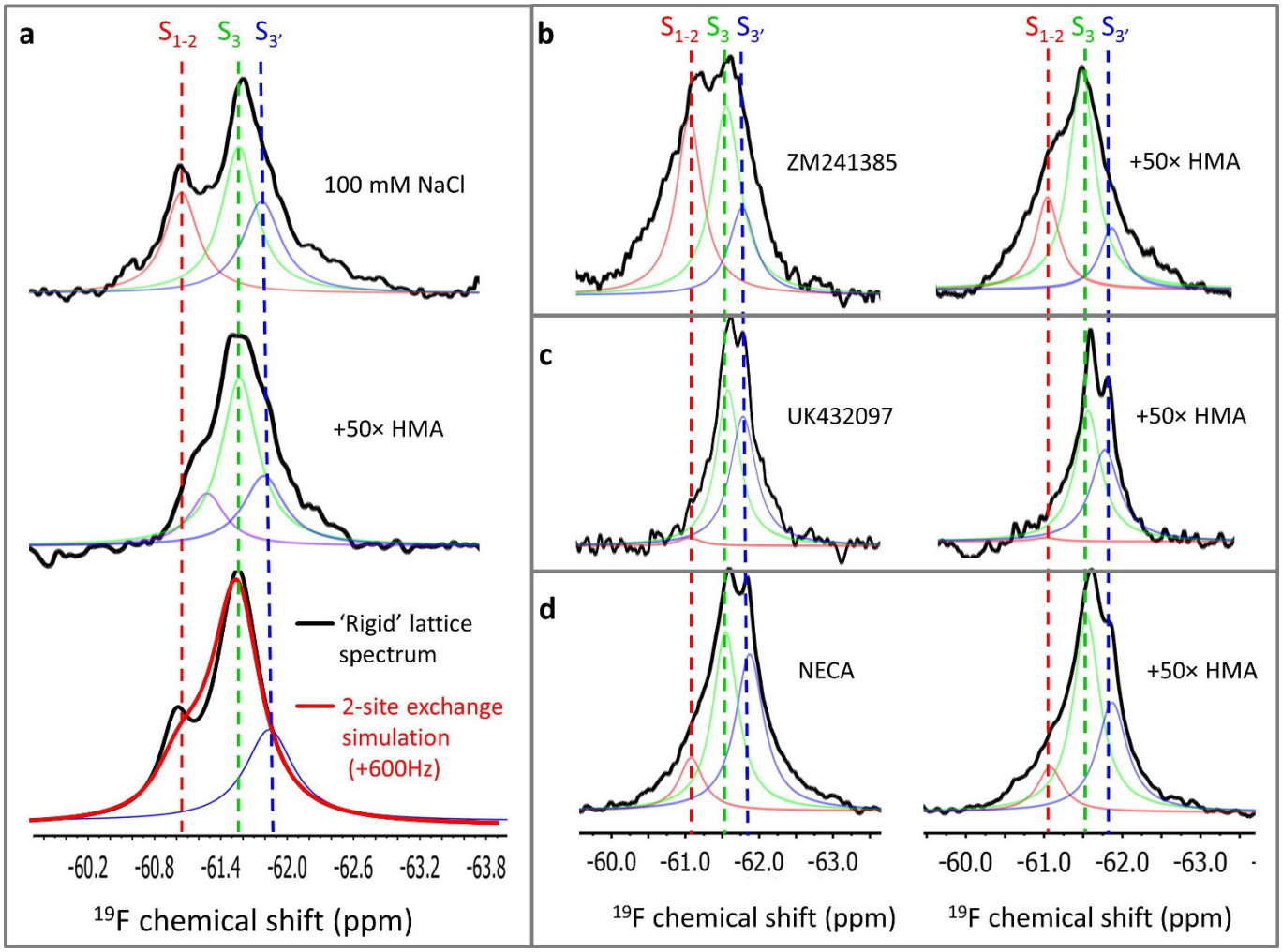

Extended Data Figure 7 | The role of HMA in the receptor activation process. a, ^{19}F NMR spectra of ^{19}F-labelled apo A_{2A}R-V229C and ^{19}F-labelled A_{2A}R-V229C in the presence of saturating amounts of the amiloride ligand 5-(*N*,*N*-hexamethylene) amiloride (HMA). Addition of 50-fold excess of HMA results in an increase in the S_3 fraction and an apparent exchange broadening and slight coalescence of S_{1-2} and S_3, which are represented by the deconvolutions in lavender and green, respectively. After accounting for the exchange process between S_{1-2} and S_3 by assuming $k_{ex} = 600$ Hz, the simulated spectrum (shown in red) compares favourably with the observed spectrum. If we assume that exchange between S_{1-2} is slow, we then obtain the 'rigid' lattice spectrum, shown in black. **b**–**d**, ^{19}F NMR spectra of ^{19}F-labelled A_{2A}R-V229C showing the effect of the addition of 50-fold excess of HMA to saturating amounts of inverse agonist (100 × ZM241385) and agonist (50 × UK432097 or 100 × NECA). In all cases, addition of HMA competes with the bound ligand and establishes a greater fraction of the S_3 state. The three deconvolved resonances are shown in red, green, and blue.

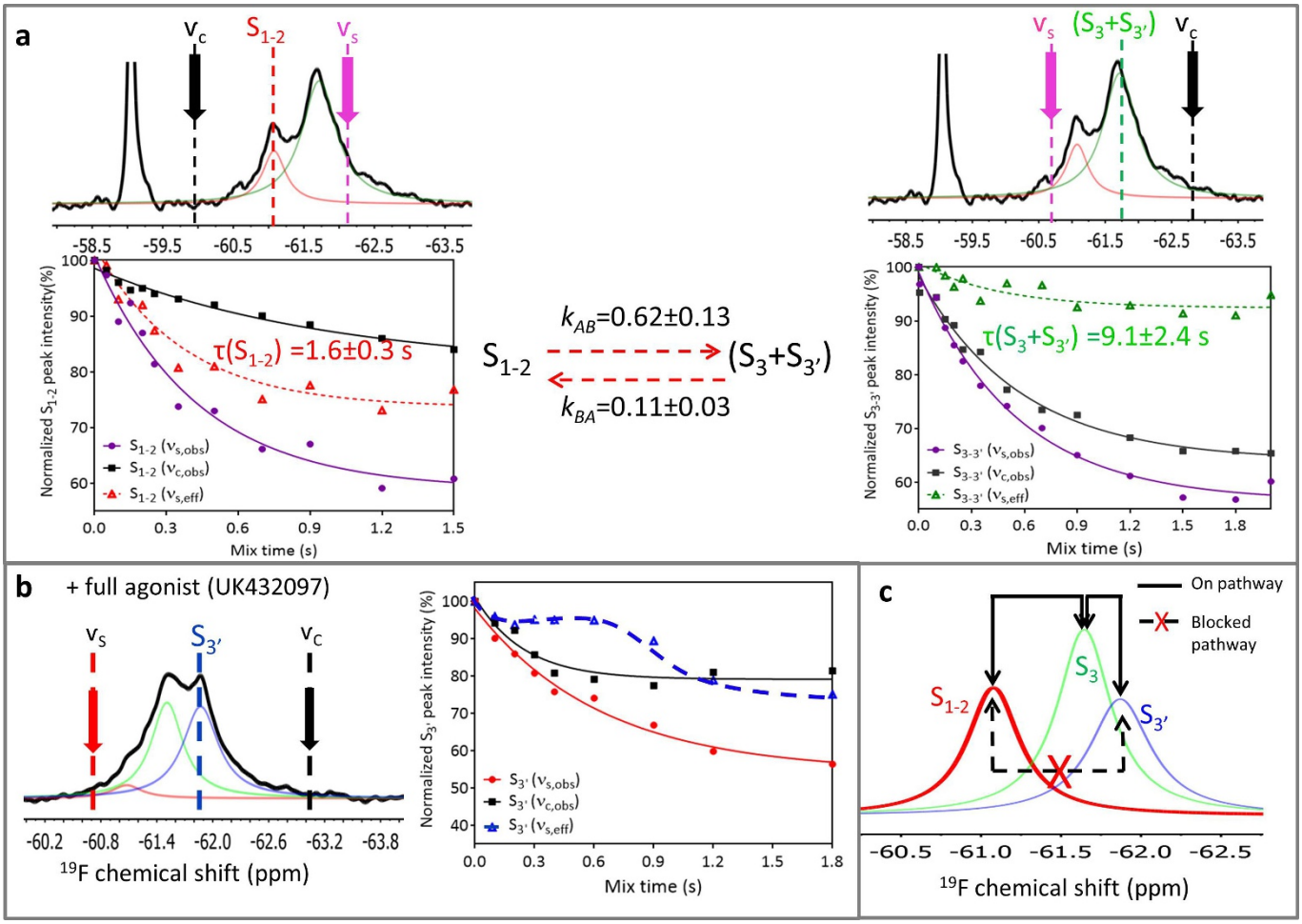

Extended Data Figure 8 | Saturation transfer experiments of ^{19}F-labelled A_{2A}R-V229C. a, ^{19}F NMR spectra of ^{19}F-labelled apo A_{2A}R-V229C with corresponding decay curves associated with continuous wave saturation of either the active state ensemble, $S_3 + S_{3'}$, or the inactive state ensemble, S_{1-2}, are provided in the left and right columns, respectively. To account for off-resonant saturation effects, a control experiment was performed at a frequency, ν_c, such that the peak of interest was equidistant to the saturation frequency, ν_S, and the control frequency, ν_c. The response of the peak of interest (that is, S_{1-2} and $S_3 + S_{3'}$ in the left and right panels, respectively) to saturation at the control frequency, ν_c, is represented by black squares. Similarly, the response of the peak of interest to saturation at ν_S is shown in violet while the effective responses, accounting for off-resonant saturation, are shown in red (S_{1-2}) and green ($S_3 + S_{3'}$). On the basis of the effective decay profiles, and using a two-site exchange model, the lifetime of the inactive state ensemble and active states is estimated to be 1.6 s and 9 s. Spectral deconvolutions allow us to estimate the populations, $p(S_{1-2})$ and $p(S_3 + S_{3'})$, to be 0.28 and 0.72, respectively. Using the fitted forward rate constant, $k_{AB} = 0.62\ s^{-1}$, the reverse rate constant is estimated to be $k_{BA} = 0.24\ s^{-1}$, assuming $k_{AB} \times p(S_{1-2}) = k_{BA} \times p(S_3 + S_{3'})$. In contrast, the response to the saturation of S_{1-2} provided an estimate of $k_{BA} = 0.11 \pm 0.03\ s^{-1}$. **b**, Saturation transfer experiments of full agonist UK432097-bound ^{19}F-labelled A_{2A}R-V229C. The effective decay curve (blue dashed line), associated with saturation of S_{1-2} is consistent with a process where $S_{3'}$ magnetization is exchanged with S_{1-2} via S_3, as suggested by the figure in **c**. **c**, Model for presumed exchange pathway between S_{1-2}, S_3, and $S_{3'}$.

Extended Data Table 1 | Primers/gene fragments used to construct plasmids for this study

Primer/ fragment	Sequences	Constructs
TEV fragment	5'-TCTAACAACAACAACAACAACAACAACAACAACAACCTTGGCGA AAACTTGTATTTCCAGGGCGCT-3'	pPIC9K_Fα-Factor–Flag–TEV-A2aARTr316-H10
PicP1-J	5'-ATTCGAAGGATCCAAACGATGAGATTTC-3' (BamHI)	pPIC9K_Fα-Factor–Flag–TEV-A2aARTr316-H10
PicP2-J	5'-GTTGTTGTTGTTGTTAGACTTATCGTCATCGTCCTTGTAGTCTC-3'	pPIC9K_Fα-Factor–Flag–TEV-A2aARTr316-H10
PicP3-H	5'GGACGATGACGATAAGTCTAACAACAACAACAACAACAACAACAACA AC-3'	pPIC9K_Fα-Factor–Flag–TEV-A2aARTr316-H10
PicP41-H	5'- TGCCTTGAAAGGTTCTTGCTGCC-3'	pPIC9K_Fα-Factor–Flag–TEV-A2aARTr316-H10
PicP4-H	5'-ATTCGCGGCCGCTCAGTGATGGTGATGGTGATGGTGATGGTG ATGTGCCTTGAAAGGTTCTTGCTGCC-3' (NotI)	pPIC9K_Fα-Factor–Flag–TEV-A2aARTr316-H10
P_{A2a_V229C}	5'- CCACACTGCAGAAGGAGTGCCATGCTGCCAAGTCAC-3'	pPIC9K_Fα-Factor–Flag–TEV-A2aARTr316-H10_V229C
PF_{AOX1}	5'- GACTGGTTCCAATTGACAAGC-3'	sequencing
PR_{AOX1}	5'- GGCAAATGGCATTCTGACATCCT-3'	sequencing